Crystallography and Morphology of Niobium Carbide in As-Cast HP-Niobium Reformer Tubes

KARL G. BUCHANAN and MILO V. KRAL

The microstructures of two as-cast heats of niobium-modified HP stainless steels were characterized. Particular attention was paid to the interdendritic niobium-rich carbides formed during solidification of these alloys. At low magnifications, these precipitates are grouped in colonies of similar lamellae. Higher magnifications revealed that the lamellae actually obtain two distinct morphologies. The type I morphology exhibits broad planar interfaces with a smooth platelike shape. Type II lamellae have undulating interfaces and an overall reticulated shape. To provide further insight into the origin of these two different morphologies, the microstructure and crystallography of each have been studied in detail using high resolution scanning electron microscopy, transmission electron microscopy, various electron diffraction methods (electron backscatter diffraction (EBSD), selected area diffraction (SAD), and convergent beam electron diffraction (CBED)), and energy dispersive X-ray spectroscopy.

© The Minerals, Metals & Materials Society and ASM International 2012

I. INTRODUCTION

HEAT-RESISTANT Fe-Cr-Ni-C austenitic stainless steels have become the dominant alloys for use in steam reforming and pyrolysis applications by the petrochemical industry. For example, depending on the process requirements, centrifugally cast alloy reformer tubes typically operate at temperatures between 1123 K and 1323 K (850 °C and 1050 °C) and internal pressures between 2 and 5 MPa for up to 100,000 hours. The combination of high temperatures and moderate stresses causes creep to be the dominant failure mechanism experienced in service. Initially, the HK (25 pct Cr, 20 pct Ni) alloy series replaced HT (18 pct Cr, 37 pct Ni) superalloys, providing tubes with comparable creep performance while reducing cost (due to the decrease in Ni). Subsequently, the HK series was superseded by the HP series (25 pct Cr, 35 pct Ni), which has shown higher creep strength and oxidation resistance than its predecessors. Extensive work has been carried out to optimize the microstructure of all of these alloys to maximize their high-temperature strength.

In the as-cast condition, the standard 25Cr-35Ni HP microstructure consists of a dendritic network of primary Cr_7C_3 (commonly known in the literature as M_7C_3) in an austenite matrix, which is relatively free of precipitation. On exposure to service temperatures, the primary Cr_7C_3 transforms to $Cr_{23}C_6$ and extensive secondary precipitation of $Cr_{23}C_6$ occurs within the matrix. The grain boundary carbide network is believed to inhibit grain boundary sliding, while the secondary matrix carbides obstruct dislocation motion.[1] However, due to the rapid diffusion of chromium through the austenite matrix (in comparison to vanadium, niobium, and titanium), the high coarsening rate of $Cr_{23}C_6$ causes it to possibly be the least effective of the available carbides for strengthening high-temperature stainless steels.[2] Addition of niobium, a strong carbide forming element, was reported to cause partial replacement of Cr_7C_3 with NbC (MC), refining and fragmenting the primary carbide network. The amount of replacement, refinement, and fragmentation of the as-cast carbide network is a function of the niobium content.[3] Accelerated creep testing showed that niobium-modified HP alloys have increased rupture life and lower minimum creep rates in comparison to the standard HP composition (*i.e.*, without niobium).[3] However, due to the decomposition of niobium carbide to *G* phase ($Ni_{16}Nb_6Si_7$) during exposure to elevated temperatures, the long-term strengthening effect of niobium is relatively unknown.

In the present work, the microstructures of two as-cast niobium-modified HP alloys were characterized with specific attention being paid to the primary NbC precipitates. Past studies described these precipitates as having a lamellar or "Chinese-script" morphology.[3–5] However, the present high-resolution scanning electron microscope observations of the primary NbC revealed that the lamellae actually take on two significantly different morphologies. The type I lamellae exhibit broad planar interfaces with a smooth platelike shape. Type II lamellae have undulating interfaces and an overall reticulated shape. The morphology of the NbC is likely to influence the NbC/G-phase transformation during the alloys exposure to service temperatures and subsequently affect the creep properties. Therefore, to provide further insight into the origin of these two different morphologies, the microstructure and crystallography of each have been studied in detail using high resolution scanning electron microscopy, transmission

KARL G. BUCHANAN, Doctoral Candidate, and MILO V. KRAL, Professor, are with the Department of Mechanical Engineering, University of Canterbury, Private Bag 4800, Christchurch, New Zealand. Contact e-mail: milo.kral@canterbury.ac.nz
Manuscript submitted December 1, 2010.
Article published online January 19, 2012

electron microscopy, various electron diffraction methods (electron backscattered diffraction (EBSD), selected area diffraction (SAD), and convergent beam electron diffraction (CBED)), and energy dispersive X-ray spectroscopy.

II. EXPERIMENTAL PROCEDURE

Two melts of HP-niobium steel were centrifugally cast in the form of tubes by Kubota Metal Corporation (designated KHR35C) and Paralloy (designated H39W). The chemical composition of each melt is listed in Table I. Samples of reformer tube were mounted for radial view (through wall) using Buehler Probemet and underwent grinding steps using 240, 400, and 600 grit silicon carbide paper and polishing steps using 9-, 3-, and 1-μm diamond paste. Prolonged final polish (4 to 5 hours) using 0.02-μm colloidal silica was necessary to remove the surface deformation induced by the previous polishing steps. For EBSD and energy dispersive X-ray spectroscopy (EDS), samples were etched for 20 seconds in glyceregia (30-mL glycerol, 30-mL HCl, and 10 mL HNO_3) and examined at 20 keV using a JEOL* JSM 6100[6] scanning

*JEOL is a trademark of Japan Electron Optics Ltd., Tokyo.

electron microscope (SEM) equipped with the Oxford eXL EDS system and HKL Technology EBSD system (Oxford Instrument, Bucks, UK).[7] Samples for high resolution scanning electron microscopy were observed in the as-polished condition, after etching for 45 seconds and after deep etching for up to 90 minutes in glyceregia. Observations of these samples were carried out at 20 keV using a JEOL 7000F[6] field emission scanning electron microscope equipped with a JEOL JED-2300 EDS detector.

For transmission electron microscopy (TEM), 3-mm-diameter discs were mechanically punched and ground to approximately 100 μm using 1200 and 4000 grit silicon carbide paper. Prior to ion milling, the specimens were electropolished in a solution of 6 pct (by volume) perchloric acid, 35 pct n-butyl alcohol, and 59 pct methanol at approximately –40 °C, a voltage of 40 V, and current of 25 mA using a E.A. Fishione automatic twin-jet electropolishing apparatus (www.fischione.com/ 9003 Corporate Circle Export, PA). Strict control of the electrolyte temperature (within ±5 °C) to maintain the potential of 40 V and 25 mA reduced the prevalence of pitting. Optimally, electropolishing was stopped just prior to perforation of the foil. Subsequent perforation and thinning to electron transparency was carried out using the Gatan precision ion polishing system[8] with an initial accelerating voltage of 3.5 keV and sputtering

angle of 6 deg. Milling was halted once the perforation began to noticeably increase in size. The accelerating voltage was reduced to 1.5 keV and the sputtering angle to 4.5 deg to grow the perforation to a suitable size (~0.2- to 0.5-mm diameter). Final cleaning of the sample at 0.5 keV and sputtering angle at 4.5 deg was carried out for 30 minutes. Analytical transmission electron microscopy (TEM) was carried out using a PHILIPS**

**PHILIPS is a trademark of FEI Company, Hillsboro, OR.

CM200[9] operated at 200 keV and equipped with an Oxford INCA x-sight EDS system.[7]

EBSD patterns (or EBSPs) were recorded in spot mode and indexed using crystallographic parameters from the Pearson's Handbook.[10] EBSPs were obtained from the primary NbC precipitates and the austenite matrix directly adjacent to each precipitate. Using HKL Technology's[7] Flamenco software, the Euler angles (φ_1, φ_2, Φ) describing the crystallographic orientation of the phase with respect to a reference axis system could be calculated. These angles were used to calculate a 3×3 orientation matrix for each analysis point, and subsequently, the misorientation between any two points could be calculated using the following matrix operation:

$$[A][B]^{-1} = [M]$$

where A and B are the orientation matrices of locations in phases A and B and M is the misorientation matrix:

$$[\mathbf{M}] = \begin{bmatrix} m_{11} & m_{12} & m_{13} \\ m_{21} & m_{22} & m_{23} \\ m_{31} & m_{32} & m_{33} \end{bmatrix}$$

The orientation relationship (OR) between location A and B is then:

$$\begin{array}{ll} [m_{11}\, m_{21}\, m_{31}]_A & // \quad [1 \quad 0 \quad 0]_B \\ [m_{21}\, m_{22}\, m_{23}]_A & // \quad [0 \quad 1 \quad 0]_B \\ [m_{31}\, m_{32}\, m_{33}]_A & // \quad [0 \quad 0 \quad 1]_B \end{array}$$

The misorientation angle θ and axis $[u\, v\, w]$ between points A and B can also be calculated using the following equation:

$$\theta = \cos^{-1}\left(\frac{m_{11} + m_{22} + m_{33} - 1}{2}\right)$$

$$[u\, v\, w] = [m_{23} - m_{32} \quad m_{31} - m_{13} \quad m_{12} - m_{21}]$$

Table I. Chemical Composition of the As-Cast HP-Niobium–Modified Alloys as Determined by Inductively Coupled Plasma Spectroscopy (Weight Percent)

Wt Pct	C	Ni	Cr	Nb	Si	Mn	Mo	V	W	Co	Fe
KHR35C	0.41	33	25	0.77	1.26	0.6	0.24	0.07	0.35	0.11	bal
H39W	0.38	32.2	24.5	0.92	1.53	1.09	0.12	0.06	0.08	0.17	bal

By considering the 24 crystallographic equivalents for the cubic system, the disorientation (*i.e.*, the variant with the smallest value of θ about axis UVW) can be determined.[11] Alternatively, the Euler angles can be converted to a quaternion representation of the crystals' orientation with respect to the reference axis. The misorientation and disorientation can be calculated following the procedures used by Sutton and Balluffi[12] and Hanson.[13] A minimum of two precipitate-matrix pairs were analyzed within each dendritic group of NbC precipitates, and over 100 groups were analyzed. Since separate plates within a particular dendritic group were similarly orientated, an average orientation was calculated for each group.

TEM trace analysis was performed on nine NbC precipitates (each from a separate dendrite group) following the processes described by Hirsch *et al.*[14] and Loretto.[15] The purpose of the trace analysis was to determine whether the plates obtained a particular crystallographic "habit plane." A minimum of three and maximum of four zone axes were indexed for each precipitate and, after correction for rotation, superimposed onto the TEM bright-field image taken at each orientation.

III. RESULTS AND DISCUSSION

Figures 1(a) and (b) show the through-wall grain structure of the two as-cast HP-niobium alloys. Depending on the centrifugal casting conditions (for example, pouring temperature and cooling rate), reformer tubes exhibit either a completely columnar or a mixed columnar-equiaxed grain structure.[16,17] The high cooling rate induced during casting of these alloys has resulted in 100 pct columnar grain structures. Qualitatively, the KHR35C alloy can be seen to have a significantly larger grain size than the H39W alloy. Figures 2(a) and (b) are scanning electron micrographs showing the as-cast microstructure of each alloy. The dendritic structure, typical of these centrifugally cast alloys, contains alternating interdendritic groups of the primary carbides Cr_7C_3 (dark gray) and NbC (white) in an austenitic matrix. EBSD was employed to identify all three as-cast phases. At the magnifications shown in Figures 2(a) and (b), the primary NbC precipitates can be seen to exhibit the typical lamellar or "Chinese–script" morphology, as described by previous studies.[3–5]

Observations of the primary NbC at higher magnifications revealed the existence of two significantly different morphologies of individual plate lamella (Figures 3(a) and (b)). Type I lamellae, shown in Figure 3(a), exhibit a relatively planar interface with the austenite. In contrast, type II lamellae exhibit significant undulations along their surfaces, as shown in Figure 3(b). In two dimensions, the type II lamellae appear somewhat fragmented. SAD and CBED analysis of thin foils confirmed that both morphologies have the fcck NbC (or MC) crystal structure. However, EDS consistently revealed small concentrations of molybdenum in type II (Table II) but none in type I. During solidification, partitioning molybdenum could have
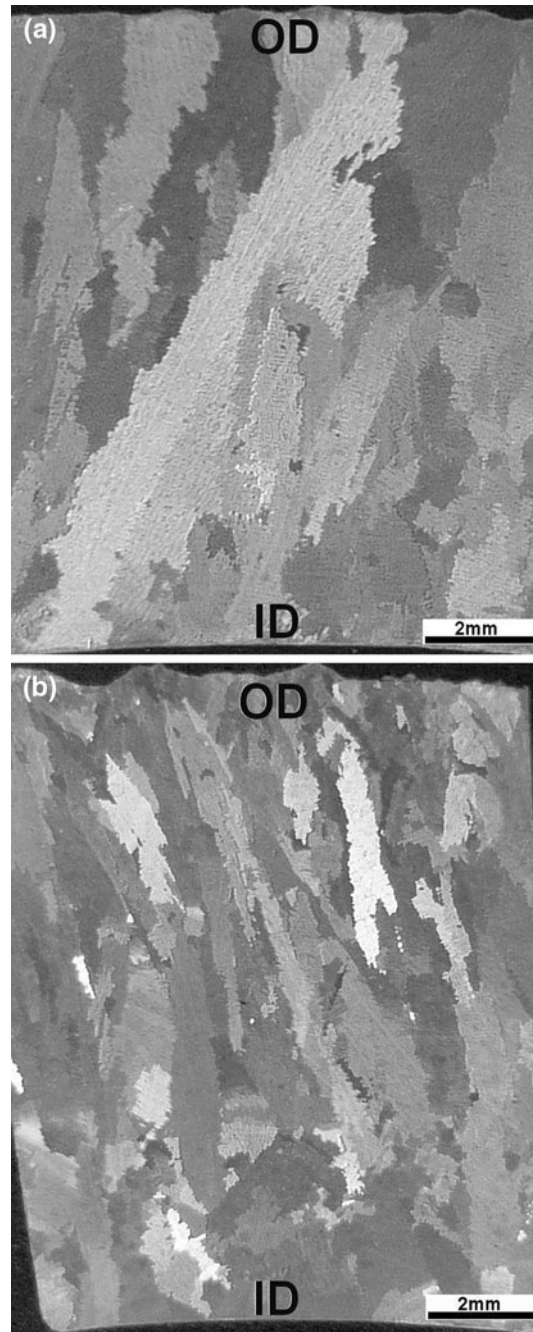

Fig. 1—Low-magnification optical micrographs showing the macrostructure of (*a*) KHR35C and (*b*) H39W (etchant: Marbles reagent).

influenced the growth morphology of the NbC precipitate; however, further investigation is required to investigate this theory. Small concentrations (<5 wt pct) of elements such as titanium (commonly utilized in combination with niobium in the HP-micro variant) were reported to cause the NbC morphology to change from lamellar to blocky.[4,5] Similar changes to (TaTiNb)C precipitates were attributed to small concentrations of hafnium and zirconium in directionally solidified Ni-based alloys.[18,19] Such additions are thought to increase the MC/matrix interfacial energy, causing the precipitates for the blocky morphology to
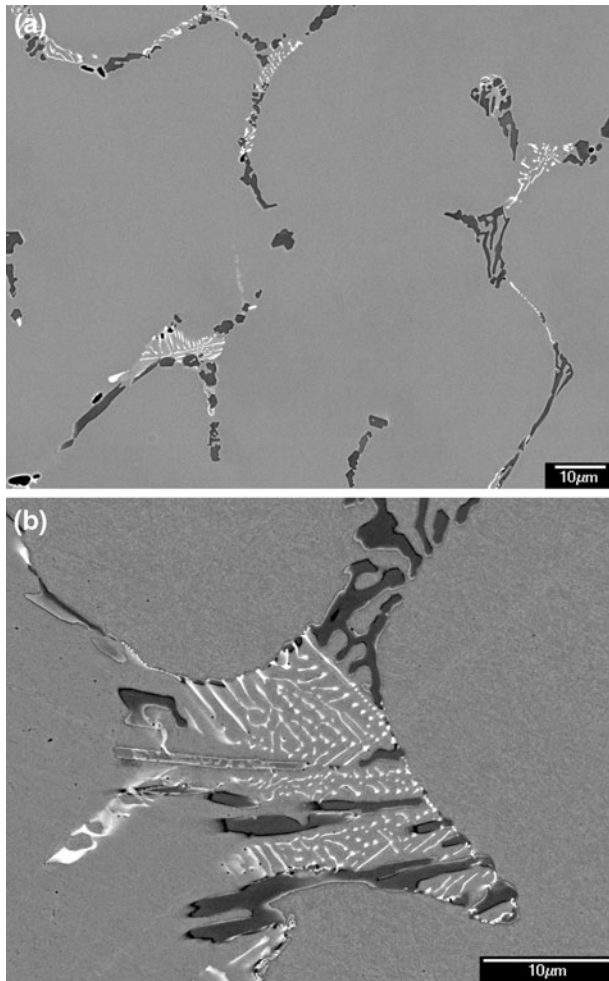
Fig. 2—Backscatter electron images of as-cast HP-niobium in the as-polished condition, with NbC appearing white and Cr_7C_3 as dark gray in an austenite matrix.

Fig. 3—Scanning electron micrographs showing the two-dimensional morphology of (*a*) type I lamellae and (*b*) type II lamellae.

minimize the interfacial area. Thus, local differences in the Mo concentration may have a smiliar modifying effect on the NbC morphology.

A small (typically <0.5-μm diameter) chromium-carbon–rich phase was observed between the type II NbC and austenite phases (Figures 4(a) and (b)). Convergent beam electron diffraction (CBED) analysis of this phase confirmed the orthorhombic Cr_7C_3 crystal structure (the same structure as the larger primary Cr-rich carbides). The Cr_7C_3/austenite interface was highly faceted. Although the dendritic groups of primary Cr_7C_3 and NbC are commonly interlinked (Figures 2(a) and (b)), it is believed that the interfacial Cr_7C_3 is independent of the primary Cr_7C_3 network (*i.e.*, the interfacial Cr_7C_3 is not caused by two-dimensional sectioning of small segments of the primary Cr_7C_3 network).

Studies of material subjected to unstressed aging for 1000 hours at 1173 K (900 °C)[20] previously reported the presence of $Cr_{23}C_6$ precipitates (typically 1 to 5 μm in diameter) on the interface of NbC lamella, which had partially transformed to *G* phase. This $Cr_{23}C_6$ precipitation was said to have formed due to the rejection of carbon from the transforming NbC precipitate into the
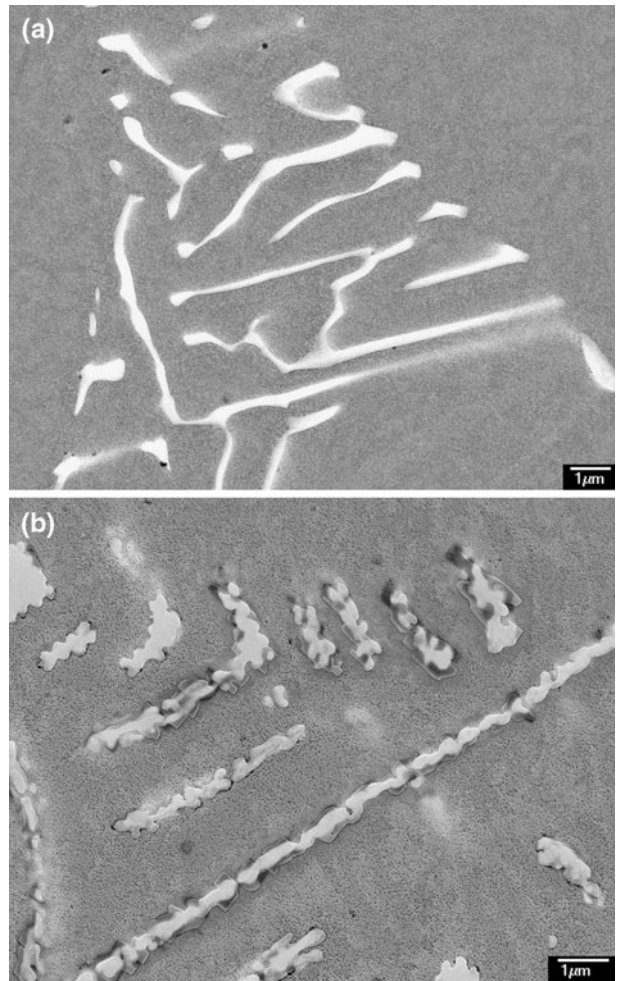
chromium-rich austenite. However, the present work suggests that these $Cr_{23}C_6$ precipitates are just as likely to have arisen due to transformation of the pre-existing interfacial Cr_7C_3 to $Cr_{23}C_6$.

The difference between morphologies becomes more apparent after deep etching (Figures 5(a) through (d)). Progressive etching experiments on the as-cast material determined that deep etching with glyceregia caused the sole dissolution of the austenite matrix while leaving the primary carbides completely intact; *i.e.*, the carbide morphologies observed were not influenced by the etching process.

Type I lamellae are revealed as smooth solid plates in three dimensions (Figure 5(a)), where the broad faces exhibit varying degrees of curvature. Small steps or facets on the broad faces of the plates (which would be associated with the curvature) were not resolved using an SEM (Figure 5(b)).

Figures 5(c) and (d) show the weblike or reticulated shape of the type II lamellae in three dimensions. The fragmentation of the lamellae observed in two dimensions (Figure 3(b)) corresponds to the three-dimensional pores within the plane of the plates. The undulations commonly occurred at a near-constant length scale

Table II. SAD and CBED Determined Crystal Structure and EDS Chemical Composition for Each NbC Morphology

Type	Crystal System	Space Group	a (nm)	Nb	Cr	Fe	Ni	V	Mo
I	fcc	$Fm\bar{3}m$	0.438	87.9	7.6	2.3	1.5	0.7	—
II	fcc	$Fm\bar{3}m$	0.440	87.2	7.4	2.5	1.7	0.6	0.6
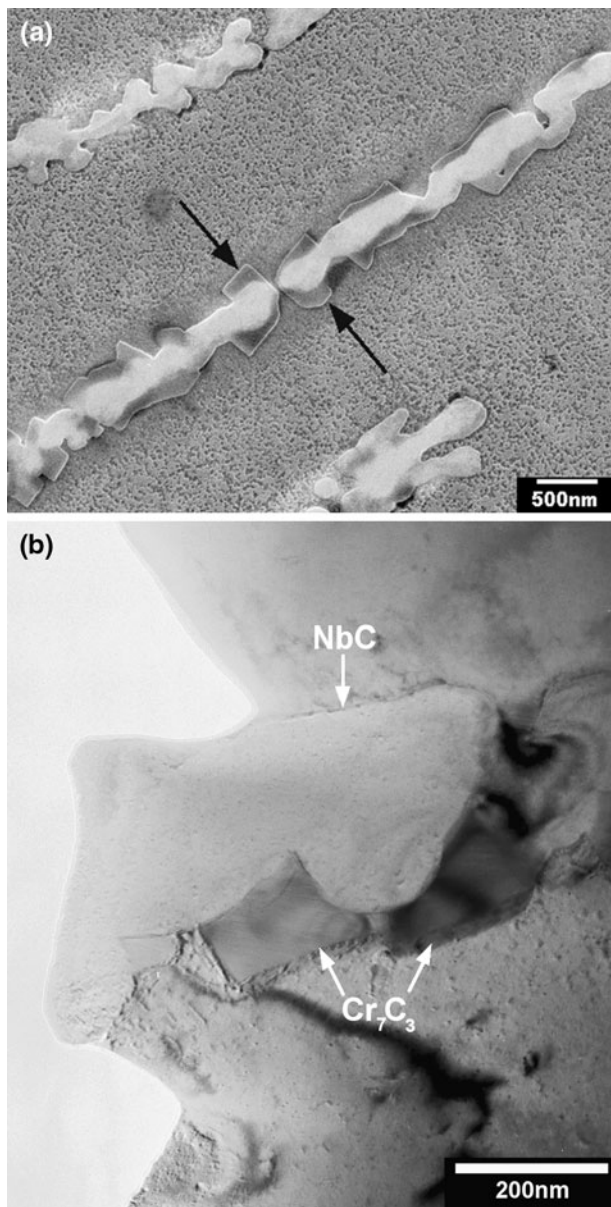
Fig. 4—(*a*) Scanning electron and (*b*) bright-field transmission electron micrographs showing the Cr_7C_3 located on the precipitate/matrix interface of type II lamellae.

causing the pore size of plates within and between separate groups to also remain consistent (typically 0.2 to 0.5 μm). Many lamellae adhered to a particular plane of growth causing the overall platelike morphology. After deep etching, the interfacial Cr_7C_3 could not be distinguished from the type II lamellae due to the lack of contrast between the two phases in scanning electron microscopy. For the H39W alloy, the type II lamellae appeared to be more prevalent than the type I lamellae

(approximately, 65 pct type II–35 pct type I). However, the type I and II lamellae appeared to be equally abundant in the KHR35C alloy (*i.e.*, 50 pct type II–50 pct type I). Neither morphology appeared to be preferentially located, *e.g.*, at dendrite, grain boundaries, or relative position within the tube wall.

The type II lamellae exhibits a higher surface area to volume ratio in comparison to the type I lamellae; however, further work (such as serial sectioning) would be required to quantify this ratio. Exposure of the alloy to temperatures between 973 K and 1323 K (700 °C and 1050 °C) causes the NbC/G-phase transformation to occur. Therefore, the total surface area and properties (*i.e.*, interfacial structure and free energy) of the as-cast NbC/austenite interface will likely influence the kinetics of the *G*-phase transformation. This transformation does not occur during thermal exposure to temperatures above 1323 K (1050 °C) (*i.e.*, the NbC phase remains stable). However, the high surface area to volume ratio could cause the type II morphology to be unstable, causing the lamellae to undergo spheroidization to reduce the total interfacial energy.

Accelerated creep testing showed that laboratory aged samples with *G* phase present increased creep ductility in comparison to samples without *G* phase.[3] Thus, the characteristics of the *G*-phase transformation are important to predicting the service behavior of these alloys. However, since the existence of these two morphologies was previously unknown in HP-niobium–modified alloys, no effort to date was made to determine the transformation characteristics specific to each morphology. Characterization of unstressed laboratory aged material is currently underway[21] to provide further insight into the importance of the morphologies.

In a study of niobium-modified HK alloys, Wen-Tai and Honeycombe[5] established the existence of a cube-cube crystallographic OR between the primary NbC and austenite:

$$\langle 100 \rangle_{NbC} || \langle 100 \rangle_{\gamma}$$
$$\{100\}_{NbC} || \{100\}_{\gamma}$$

Calculation of the OR using EBSD and the matrix operations described in the experimental procedure confirmed that all type I lamellae located at dendrite boundaries obtain this cube-cube OR (on all sides of the lamella) with the austenite matrix. In cases where the lamellae were located on grain boundaries, the OR was exhibited with the grain, which contained the associated colony of lamellae (*i.e.*, the grain where nucleation of the colony occurred). The histogram in Figure 6(a) shows the magnitude of disorientation for each precipitate-matrix pair. Thirty-one out of the 40 precipitate type I groups analyzed were found to deviate from this ideal
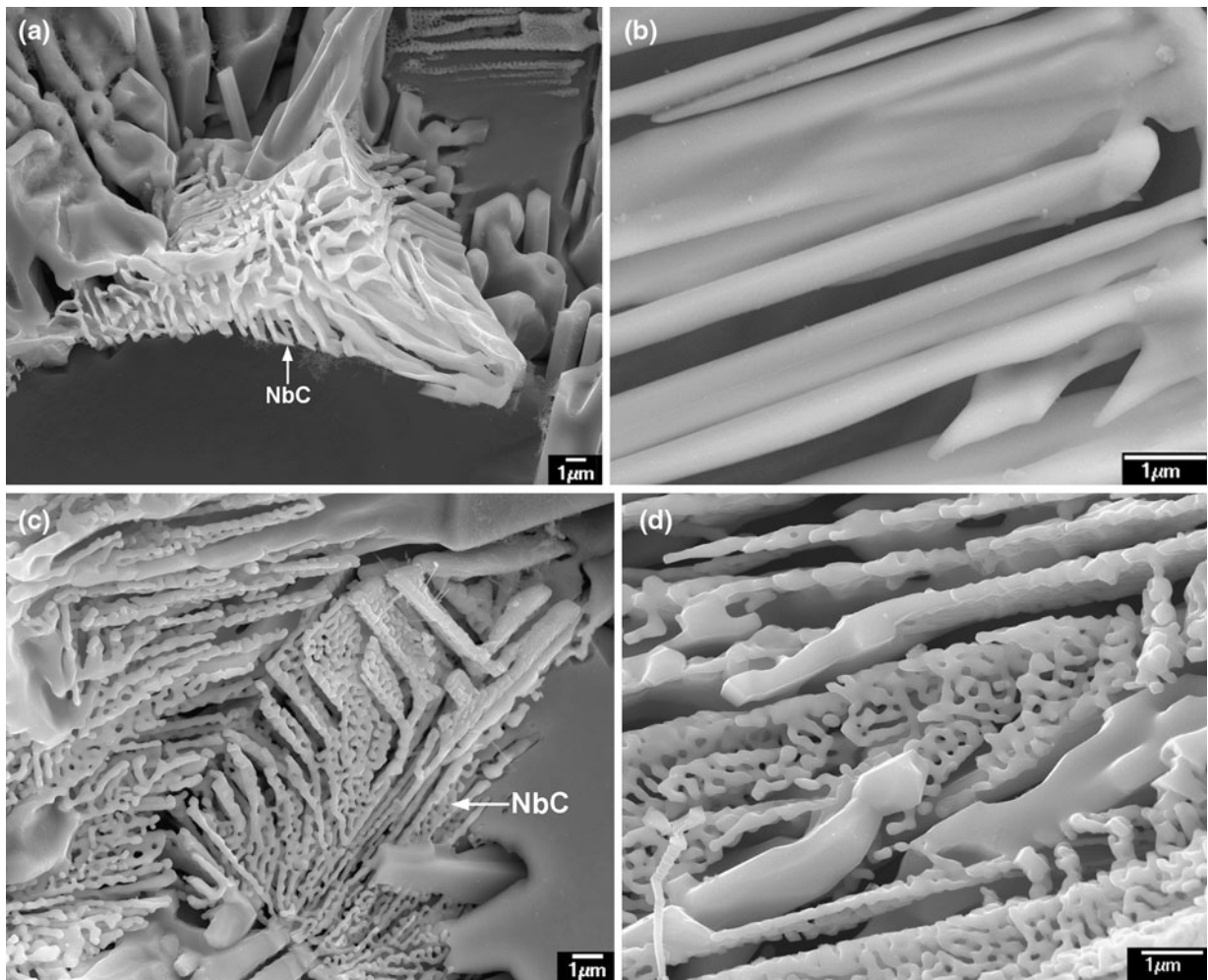
Fig. 5—Three-dimensional morphology of (*a*) and (*b*) type I lamellae and (*c*) and (*d*) type II lamellae.

relationship by less than 5 deg. All precipitates within a single group had the same crystallographic OR with a typical variance of less than 1 deg.

A similar analysis for the type II lamellae yielded complex expressions of OR such as

$$[\overline{25}\,\overline{1}\overline{3}25]_{NbC}||[10\,0]_{\gamma}$$
$$[11\overline{2}50]_{NbC}||[010]_{\gamma}$$

Although a consistent (but complex) crystallographic orientation relationship may exist between this example precipitate-matrix pair, rational pairs of parallel planes and directions from this information are not obvious. Therefore, calculation of the disorientation for each precipitate-matrix pair was performed to determine if clustering around a common angle occurred. Crystallographic orientation relationships with disorientations matching this common disorientation angle could then be confirmed or rejected by plotting the crystal pair with respect to each other in a stereographic projection and checking if the candidate poles were coincident.

Precipitates within each single group of type II lamellae were found to share a similar orientation with respect to the matrix (typical disorientation variance of

less than 1 deg). However, between groups, the disorientation varied significantly (Figure 6(b)). The high level of variance between groups of these precipitates indicates that they are not likely to obtain a consistent orientation relationship with the matrix. Though there may seem to be slight clustering around 55 deg, it must be noted that these plots only display the magnitude of disorientation and not the axis of rotation. This axis was found to vary considerably when comparing precipitate-matrix pairs with a disorientation of approximately 55 deg.

TEM trace analysis of linear/planar features was performed to determine if the type I and II lamellae obtain a specific crystallographic habit plane. For the type I lamellae, traces were taken along the broad faces of lamella, which had a sufficient linear edge (such as the precipitate shown in Figure 7(a)). The traces taken from four widely separated zone axes for this precipitate are plotted on the stereographic projection shown in Figure 7(b). Each trace can be seen to intersect at the (100) pole. The linear edges of three type I lamellae were examined, all of which exhibited a {100} habit plane.

The traces determined from the type II lamella shown in Figures 8(a) and (b) are plotted in Figure 8(c). As the precipitates had no linear edge from which to take the
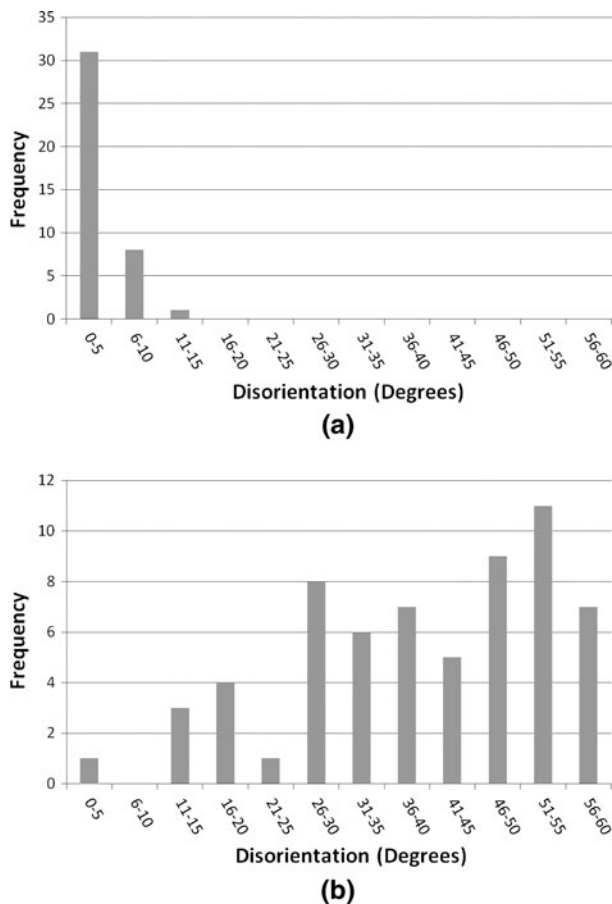
Fig. 6—Histograms showing the frequency of occurrence of disorientation measured between NbC-matrix pairs for the (a) type I lamellae and (b) type II lamellae.

traces, an estimated centerline for each lamella was defined as the trace direction. As shown in Figure 8(c), the general area of intersection of the traces shows no strong association with any low index habit plane. Furthermore, the area of intersection for each set of traces was inconsistent. Trace analysis was performed on five type II lamellae, each showing similar inconsistencies, indicating that it is unlikely that these plates obtain a rational habit plane over large areas. However, the complex shape of these precipitates and the presence of the interfacial Cr_7C_3 causes great difficulty when attempting to consistently determine the trace direction when viewing the precipitate from different crystallographic orientations. Analysis of deviations in the measured trace direction of approximately 5 deg resulted in a worst case intersection deviation on the stereographic projection of 10 to 15 deg. Therefore, the sum of small errors in defining the trace for each zone could be largely attributed to the resulting ambiguities on the stereographic projection.

While the type II morphology was not reported for Nb-rich MC precipitates in HP or HK alloys, similar morphologies were observed in directionally solidified and single-crystal Ni-based alloys.[22–24] Tin and Pollock[22,23] identified three distinctly different morphologies (blocky, Chinese-script, and nodular), which

Ta-rich MC precipitates exhibited in various single-crystal Ni-based alloys. In all alloys with carbon additions, the script and nodular lamellae were dominant, with only few blocky precipitates typically observed. The ratio of script to nodular precipitates varied significantly with respect to overall alloy composition. However, no single alloying element could be attributed to altering the script-nodular preference. While both morphologies existed throughout the cross section, the nodular TaC precipitates were the sole precipitates situated around freckle chain defects. These defects are a direct result of compositional gradients within the "mushy zone," indicating the importance of local melt composition with respect to morphology. While the overall solidification conditions were kept constant, local variations were present due to the turbine blades complex geometry. However, these local variations did not significantly affect the script-nodular preference.

The morphological dependence of MC carbides with respect to the solidification conditions was studied extensively in directionally solidified (DS) Ni-based alloys.[24–30] Typically, individual studies kept the overall alloy composition constant while varying the solidification conditions at the γ/L interface. Due to the large range of Ni-based alloys, the MC composition varied significantly between studies (for example, (TaTi)C,[24] (TiMo)C,[25] (NbTi)C,[29] and (NbTiW)C[32]). Although composition is known to affect the MC morphology,[4,18,19] generally all MC compositions followed similar trends with respect to the solidification conditions.

Previous work has shown that the thermal gradient at the γ/L interface (G_L) and overall growth rate (R) play an important role in determining the morphology of the advancing γ/L interface, thus influencing the MC growth characteristics. In general, blocky morphologies dominated at high G_L/R ratios while low ratios promoted script morphologies similar to the type I lamellae. When G_L remained constant, the MC precipitates formed blocky morphologies at growth rates below 5 μm/s, which progressively transitioned to script morphologies at growth rates between 5 to 100 μm/s.[19,23–26,28] The exact growth rate where the transition occurred in each Ni-based alloy was specific to the composition of the MC precipitate. Under splat cooling conditions, fine faceted blocks (thought to be present in the melt prior to quenching) were dominant.[19,27] Melt treatments such as superheating were also reported to induce the blocky to script transition.[30]

Low growth rates ($R < 1$ μm/s) induced planar growth fronts where nucleation and growth of the blocky precipitates occurred in the liquid ahead of the advancing γ/L interface. These blocky MC precipitates typically exhibited the equilibrium octahedral shape.[19,23,26,27] Cellular growth fronts occurred at intermediate growth rates ($1 < R < 5$ μm/s) with the MC precipitates exhibiting irregular blocky or elongated platelet morphologies.[19,24,27–29] This irregular shape often appeared to be a transitional morphology where both blocky and scriptlike features could be identified. In some cases, the irregular morphologies contained
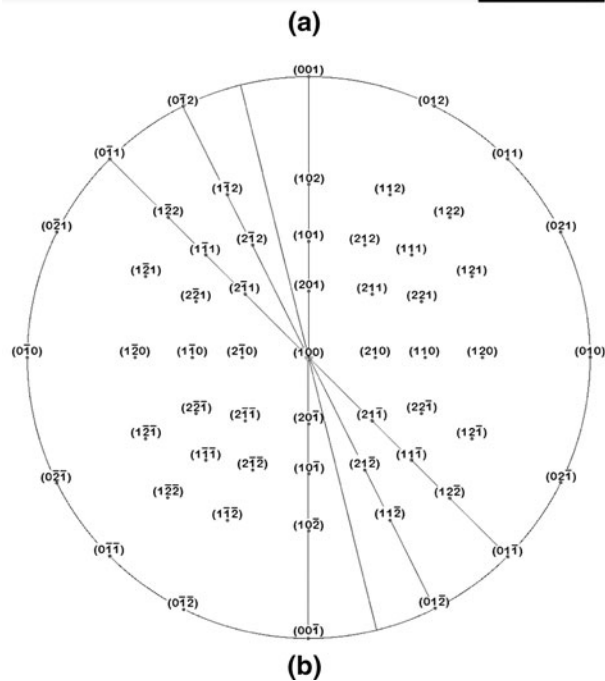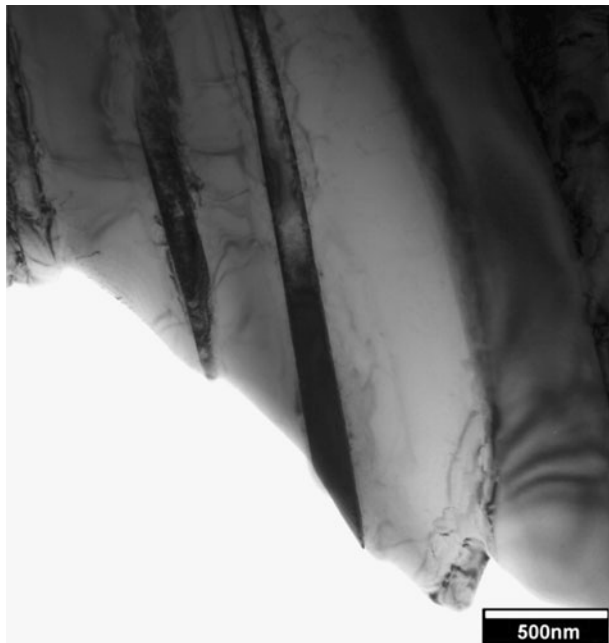
Fig. 7—(a) Representative bright-field transmission electron micrograph of the type I lamellae. (b) Stereographic projection centered about $(100)_{NbC}$ showing the intersection of four traces taken from (a).

titanium-nitrogen or hafnium-rich cores, which had heterogeneously nucleated on aluminum or magnesium oxide melt inclusions.[25,26,29] Dendritic growth fronts associated with higher growth rates ($R > 5$ μm/s) resulted in higher levels of solute supersaturation within the interdendritic regions, promoting the formation of a MC/γ eutectic. The favorable conditions for the growth of dendritic carbide branches result in the Chinese-script morphology.[19,24,27,28] Existing octahedral precipitates were also observed to preferentially grow along the

$\langle 100 \rangle_{MC}$ direction, resulting in arrowhead-shaped plates or rods.[19,23,26]

Although script morphologies similar to the type I lamellae were commonly observed in DS Ni-based alloys, morphologies similar to the type II lamellae were rare. Nodular rods rich in titanium and tantalum were observed on the grain boundaries of a DS alloy when the growth rate was reduced below 0.5 μm/s.[24] These rods were thought to have grown ahead of the γ/L interface into the solute-rich liquid until the MC + γ eutectic composition was reached. Coarsening of the rod due to the eutectic reaction subsequently formed the nodules. However, no significant compositional or structural analysis was performed on the blocky, script, or nodular morphologies observed in this alloy. Thus, it is difficult to attribute the nodular rod formation to either the local solidification rate or local melt composition.

Based on the preceding observations, the type I lamellae are believed to be formed during eutectic solidification. Initially, rejection of niobium and carbon to the melt during dendritic growth of the austenite occurs until the MC + γ eutectic composition is reached. Nucleation of the type I lamella likely occurs on the existing austenite dendrite, setting the NbC/austenite orientation relationship. The {100} habit plane is formed during cooperative growth of the NbC lamellae and austenite, thus allowing the precipitates to obtain a high surface area while minimizing the total free energy associated with the boundary. These observations are consistent with those exhibited by the TaC, (TaTiNb)C, and (TiNb)C script morphologies in Ni-based alloys.[18,22,23,31–33] Preferred orientation relationships and habit planes were also observed in other alloy systems containing lamellar precipitates (for example, the Bagaryatsky or Pitsch–Petch relationships of pearlite[34]), where selection of these unique ORs and habit planes is thought to be influenced by the nucleation site, interfacial energy, and relative growth rates of the constituents.[35]

For the type II lamellae, nucleation and growth is not well understood. Similar to the blocky morphology in Ni-based alloys, the type II lamellae did not obtain an OR with the matrix, suggesting that these precipitates also form in the liquid ahead of the γ/L interface. The higher type II prevalence in the H39W alloy indicates that higher niobium contents (when comparing the H39W and KHR35C alloys, Table I) further promote nucleation in the liquid. The differing solidification conditions (as suggested by the differing grain sizes) may also influence the morphology preference; however, controlled solidification studies (where the solidification rate, thermal gradient, alloy composition, and inclusion content are systematically varied) are necessary to determine the factors that dominate the final morphology preference. While the overall alloy composition and solidification conditions likely influence the relative proportion of the type II lamellae, the present evidence (i.e., no consistent NbC/γ OR, overall planar growth, and undulations within the plates) suggests that the morphology is determined by the nucleation site and local solidification conditions.
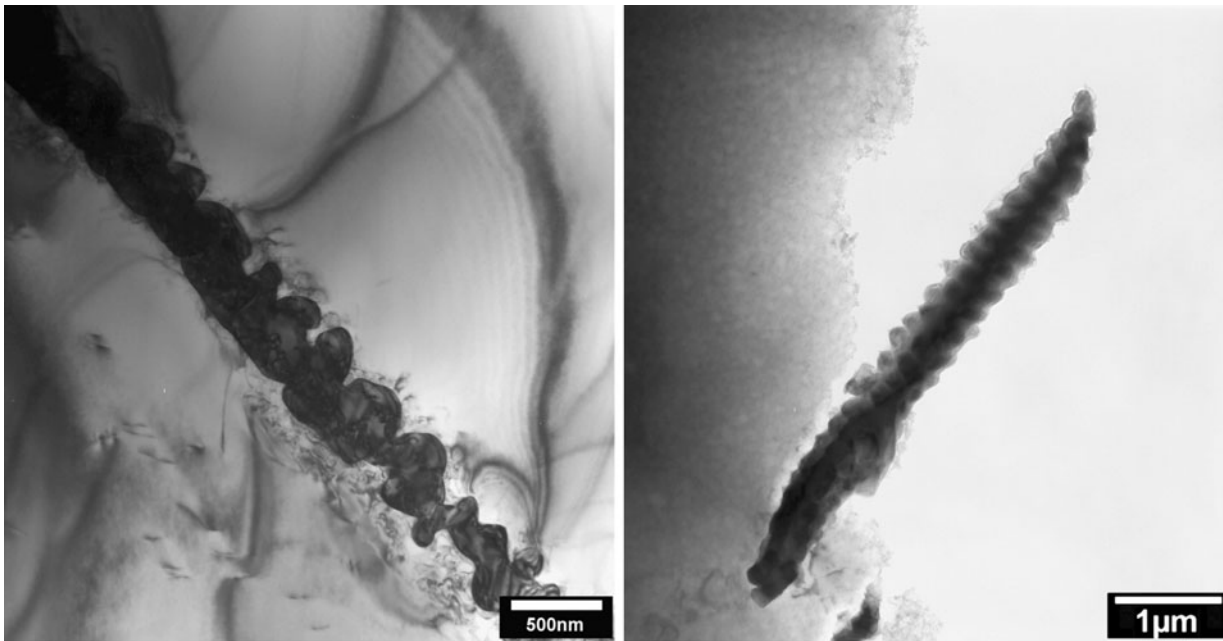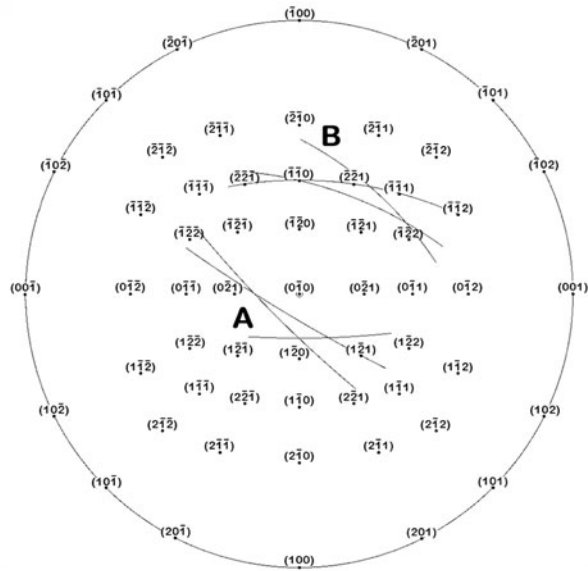
Fig. 8—(a) and (b) Representative bright-field transmission electron micrographs of the type II lamellae. (c) Stereographic projection centered about $(0\bar{1}0)_{\mathrm{NbC}}$ showing the intersections of the three traces from precipitate (a) and of the three traces from precipitate (b).

Nucleation of the type II lamellae possibly occurs heterogeneously on oxide inclusions. Spherical TiC nuclei surrounded by blocky (NbTi)C precipitates were observed in the HP-micro alloy (Nb and Ti additions) and IN718 Ni-based alloys.[17,29,36] Submicron aluminium, magnesium, and zirconium oxide inclusions were detected within these TiC nuclei, indicating the presence of Al_2O_3, MgO, or ZrO melt inclusions.[17,29,36] Nucleation of blocky (TiMo)C precipitates on alumina inclusions was also observed in directionally solidified IN100 alloys.[25] While no evidence of oxide inclusions associated with the type II lamellae was found, it is unlikely these submicron inclusions are isolated to the HP-micro

alloy. The surrounding TiC nuclei in the HP-micro alloys typically causes the inclusions to be easily distinguishable within the blocky (NbTi)C. Therefore, the absence of titanium could make it inherently difficult to locate these oxide inclusions in the HP-niobium alloys.

During growth of the blocky morphology in HP-micro, the addition of titanium possibly increases the MC/L interfacial energy. Therefore, the blocky morphology is formed to minimize the surface area to volume ratio. The type II NbC may be associated with a lower interfacial energy, allowing for the precipitates to form with significantly higher surface areas. The array of undulations within the plane of the plates is also possibly

influenced by partitioning molybdenum concentrating at the advancing NbC/melt interface. Once a threshold concentration capable of affecting the growth profile is reached, the growth direction may be forced to alter. Similar modifications of eutectic morphologies (faceted to fibrous) due to elemental poisons (such as sodium or strontium in the Al-Si system) are well known in the literature.[35] The overall planar growth of the type II lamellae is likely related to a preferred growth direction aligning with local melt thermal and chemical gradients.

IV. SUMMARY AND CONCLUSIONS

The primary NbC distribution was found to consist of two different morphologies. Both had an fcc crystal structure ($a = 0.44$ nm). No location preference of either morphology was observed with respect to dendrite boundary, grain boundary, or wall position. The attributes for each morphology can be summarized as follows.

Type I:

1. solid lamellar plates, which share a relatively planar interface with the adjacent austenite;
2. $\langle 100 \rangle_{NbC} || \langle 100 \rangle_{\gamma}$, $\{100\}_{NbC} || \{100\}_{\gamma}$ orientation relationship; and
3. exhibited a $\{100\}$ habit plane.

Type II:

1. weblike or reticulated plates, which often adhered to an overall growth plane, but exhibited no crystallographically rational habit plane;
2. no consistent, rational NbC/matrix orientation relationship;
3. more prevalent than the type I lamellae, particularly so in the H39W alloy, which contained a higher niobium content;
4. molybdenum present in the NbC composition; and
5. Cr_7C_3 identified between the NbC and austenite.

The preceding observations suggest that the morphological difference is determined by the solidification conditions that each type of lamellae experience. In the case of type I lamellae, nucleation occurs on the existing austenite dendrite followed by eutectic growth of the lamellae with the austenite. The type II lamellae likely nucleate in the liquid ahead of the γ/L interface, prior to the formation of the type I lamellae. Local melt thermal and chemical gradients subsequently dominate growth of the type II lamellae, resulting in the observed array of undulations within the plates and overall planar growth.

ACKNOWLEDGMENTS

REFERENCES

1. E.A.A.G. Ribeiro, R. Papaleo, and J.R.C. Guimaraes: *Metall. Trans. A*, 1986, vol. 17A, pp. 691–96.
2. W.-T. Hou and R.W.K. Honeycombe: *Mater. Sci. Technol.*, 1985, vol. 1, pp. 390–97.
3. G.D. de Almeida Soares, L.H. de Almeida, T.L. da Silveira I. Le May: *Mater. Charact.*, 1992, vol. 29, pp. 387–96.
4. L.H. De Almeida, A.F. Ribeiro, and I. Le May: *Mater. Charact.*, 2002, vol. 49, pp. 219–29.
5. H. Wen-Tai and R.W.K. Honeycombe: *Mater. Sci. Technol.*, 1985, vol. 1, pp. 385–89.
6. www.jeol.com.
7. www.oxford-instruments.com.
8. www.gatan.com.
9. www.fei.com.
10. P. Villars and L.D. Calvert: *Pearson's Handbook of Crystallographic Data for Intermetallic Phases*, 2nd ed., ASM INTERNATIONAL, Materials Park, OH, 1991.
11. V. Randle: *The Measurement of Grain Boundary Geometry*, Institute of Physics Pub, Bristol, PA, 1993, pp. 24–28.
12. A.P. Sutton and R.W. Balluffi: *Interfaces in Crystalline Materials*, Oxford Science Publications, Gloucestershire, 1996, pp. 17–20.
13. A. Hanson: *Visualizing Quaternions*, Morgan Kaufmann, San Francisco, CA, 2006, pp. 52–54.
14. P.B. Hirsch, A. Howie, R.B. Nicholson, D.W. Pashley M.J. Whelan: *Electron Microscopy of Thin Crystals*, 1st ed., Butterworths, London, 1965, pp. 311–15.
15. M.H. Loretto: *Electron Beam Analysis of Materials*, 2nd ed., Chapman & Hall, London, 1994, pp. 252–53.
16. X.Q. Wu, H.M. Jing, Y.G. Zheng, Z.M. Yao, W. Ke, and Z.Q. Hu: *Mater. Sci. Eng.*, 2000, vol. A293, pp. 252–60.
17. F.G. Caballero, P. Imizcoz, V. Lopez, L.F. Alvarez, and C. García de Andrěs: *Mater. Sci. Technol.*, 2007, vol. 23, pp. 528–34.
18. Q.Z. Chen, N. Jones, and D.M. Knowles: *Acta Mater.*, 2002, vol. 50, pp. 1095–1112.
19. A.K. Bhambri, T.Z. Kattamis, and J.E. Morral: *Metall. Trans. B*, 1975, vol. 6B, pp. 523–37.
20. R.A.P. Ibanez, G.D. de Almeida Soares, L.H. de Almeida, and I. Le May: *Mater. Charact.*, 1993, vol. 30, pp. 243–49.
21. K.G. Buchanan and M.V. Kral: University of Canterbury, Christchurch, New Zealand, unpublished research, 2011.
22. S. Tin, T.M. Pollock, and W. Murphy: *Metall. Mater. Trans. A*, 2001, vol. 32A, pp. 1743–53.
23. S. Tin and T.M. Pollock: *Metall. Mater. Trans. A*, 2003, vol. 34A, pp. 1953–67.
24. W.R. Sun, J.H. Lee, S.M. Seo, S.J. Choe, and Z.Q. Hu: *Mater. Sci. Eng.*, 1999, vol. A271, pp. 143–49.
25. R. Fernandez, J.C. Lecomte, and T.Z. Kattamis: *Metall. Trans. A*, 1978, vol. 9A, pp. 1381–86.
26. J. Chen, J.H. Lee, C.Y. Jo, S.J. Choe, and Y.T. Lee: *Mater. Sci. Eng.*, 1998, vol. A247, pp. 113–25.
27. L. Liu, F. Sommer, and H.Z. Fu: *Scripta Metall.*, 1994, vol. 30, pp. 587–91.
28. S.M. Seo, I.S. Kim, J.H. Lee, C.Y. Jo, H. Miyahara, and K. Ogi: *Mater. Sci. Technol.*, 2008, vol. 24, pp. 110–14.
29. A. Formenti, A. Eliasson, A. Mitchell, and H. Fredriksson: *High Temp. Mater. Process.*, 2005, vol. 24, pp. 239–58.
30. F.S. Yin, X.F. Sun, J.G. Li, H.R. Guan, and Z.Q. Hu: *Scripta Mater.*, 2003, vol. 48, pp. 425–29.
31. K.A. Al-Jarba and G.E. Fuchs: *Mater. Sci. Eng.*, 2004, vol. A373, pp. 255–67.
32. J. Yang, Q. Zheng, X. Sun, H. Guan, and Z. Hu: *J. Mater. Sci.*, 2006, vol. 41, pp. 6476–78.
33. V.A. Wills and D.G. McCartney: *Mater. Sci. Eng.*, 1991, vol. A145, pp. 223–32.
34. D.S. Zhou and G.J. Shiflet: *Metall. Trans. A*, 1992, vol. 23A, pp. 1259–69.
35. R. Elliott: *Int. Met. Rev.*, 1977, vol. 22, pp. 161–86.
36. F.C. Nunes, L.H. de Almeida, J. Dille, J.L. Delplancke, and I. Le May: *Mater. Charact.*, 2007, vol. 58, pp. 132–42.